Geometrical factors determining dendritic domain intersection between neurons: a modeling study

Rafael Ignacio Gatica[1], Trinidad Montero[1], Navid Farassat[2] and Pablo Henny[1]

[1]Laboratorio de Neuroanatomía, Departamento de Anatomía, and Centro Interdisciplinario de Neurociencia, NeuroUC, Escuela de Medicina, Pontificia Universidad Católica de Chile, Santiago, Chile

[2]Institute for Neurophysiology, Goethe University, Frankfurt, Germany

*Corresponding author:

E-mail: pablohenny@uc.cl

Keywords: Convex hull; dendritic domains; dopaminergic neurons; polyhedron intersection; in vivo neuron reconstruction.

ABSTRACT

Overlap between dendritic trees of neighboring neurons is a feature of nervous systems. Overlap allows neurons to share common afferences and defines the topography of the circuit they belong to. Proximity is also a requirement for dendritic communication, including dendro-dendritic synaptic contacts. We simulated overlap dynamics between pairs of ventral tegmental area dopamine neurons, a population characterized by diverse and extensive dendritic domains. Using each neuron's 3D convex hull (CH) as a proxy for dendritic domain size and shape, we examined intersection versus cell-to-cell distance curves for 210 pairs of neurons, and found that decay dynamics were diverse and complex, indicating that intersection between real dendritic domains does not comply with spherical or isotropic shape assumptions. We re-examined intersection dynamics for the same 210 pairs, but this time with either: a) a normalized volume corresponding to the average volume of all CHs, b) normalized shapes, using an average CH shape, or CHs from neurons exhibiting average dendritic distribution, isotropy or morphology, or c) a normalized cell body position, which we artificially placed in each CHs' centroid. All three interventions significantly increased pair intersection and simplified decay dynamics, yet shape normalization had the strongest influence. Critically, shape uniformity was also the most relevant factor for increased dendritic domain pair intersection using the neurons' original brain position and distances. We applied this experimental approach to other populations using reconstructions from neuromorpho.org database and found that shape and intersection dynamics were cell-type dependent. We conclude that intersection between neurons is not only maximized by proximity, but that individual-specific dendritic domain geometries have a profound impact too. The results predict

that one biological solution for circuits requiring selective connectivity is to exhibit greater heterogeneity in size, cell body location, and especially shape, among their constituent neuronal elements.

1. INTRODUCTION

Overlap between the dendritic trees of adjacent neurons is a common feature of the nervous system (Harris & Spacek, 2017; Nieuwenhuys et al., 1998; Ramon y Cajal, 1904). Neurons whose respective dendrites share a given locus are likely to share common afferent inputs (Braitenberg & Schüz, 1998; Packer et al., 2013; Peters & Feldman, 1976). Also, the topographical organization of a projection system is partly defined by the degree to which spatially adjacent neurons share or exclude sensory or afferent inputs (Nieuwenhuys et al., 1998). The role of dendritic fields' overlap may be particularly important in brain structures such as the neocortex of large mammals, which in large-brain exhibit a trend to decreased neuronal density (neuronal cell body density) and a more extensive neuropil (Herculano-Houzel, 2011). In addition, proximity also ensures dendro-dendritic paracrine transmission (Brombas et al., 2017; Rice & Patel, 2015) and it is a requirement for establishing dendro-dendritic synapses (Groves & Linder, 1983; Hinds, 1970). The role of dendritic overlap between adjacent neurons in determining integration or segregation of afferent signals may play is also expected to be critical in species in which neuronal density (neuronal cell bodies) decreases and neuropil increases, as it happens in the neocortex of large-brain mammals (Herculano-Houzel, 2011)

Dendritic domains overlap has been studied at a population level in somatosensory and visual systems in the context of neurons' receptive field development (Jan & Jan, 2010; Lefebvre et al., 2015; Oleson et al., 2014). In invertebrates, for instance, initial overlap between same-class dendritic arborization skin surface neurons is gradually eliminated, resulting in a complete and

64 non-overlapping coverage of the sensory surface, and similar processes have been described
65 for ganglion and some amacrine cell types in the vertebrate retina (Jan & Jan, 2010; Lefebvre et
66 al., 2012, 2015). Conversely, neurons whose function requires signal integration from multiple
67 receptive fields, as it is the case for motion detection cholinergic or dopaminergic amacrine
68 cells, exhibit dendritic domains that overlap extensively (Brombas et al., 2017; Farajian et al.,
69 2004; Keeley & Reese, 2010).
70
71 As for other central nervous system neurons, only a few studies have expressly examined and
72 reported dendritic domain overlap and its anatomical or developmental determinants. For
73 instance, overlap between mouse Purkinje cells was shown to depend on lobule location and
74 developmental stage (Nedelescu et al., 2018) and, in mouse cortical pyramidal cells, overlap
75 was shown to be severely affected following disruption of proper somatic spacing and dendritic
76 arborization development (Zhang et al., 2012)
77
78 In this study we sought to understand overlap in central nervous system neurons using a single
79 cell pair analysis approach, with which we aimed to capture the fine dynamics that underlie
80 intersection in a real, three-dimensionally organized and morphologically heterogeneous
81 population. More specifically, we sought to answer the following questions: 1) what are the
82 geometrical determinants of dendritic domain intersection between pairs of neurons in adult
83 central neurons? 2) what is the specific influence of dendritic domain size, shape and the cell
84 body placement on intersection? 3) how does cell-to-cell morphology heterogeneity affect
85 dendritic domain pair intersection dynamics?

To address these questions, we studied adult mouse ventral tegmental area (VTA) dopamine (DA) neurons, a population involved in reinforcing behavior, and whose neurons are morphologically characterized by long radiating and overlapping dendrites (Montero et al., 2021) that sub-serve integration of multiple and heterogeneous input sources (Geisler & Zahm, 2005). We used the neurons' convex hulls polyhedrons (CHPs) generated from previously 3D reconstructed VTA DA neurons (Montero et al., 2021). CHPs enclose the minimal convex volume in which the dendritic domains locate and have been used as proxies for dendritic domain size and shape (Felix et al., 2013; Gärtner et al., 2004; Gertler et al., 2008; Ito, 2020; Malmierca et al., 1995; Vrieler et al., 2019).

Consequently, in this study we set the following aims: 1) to test the assumption that CHPs are adequate proxies for dendritic domain size and shape and, similarly, that convex hulls intersections are adequate proxies for dendritic domain and proximity, 2) to model the influence of cell body to cell body distance on intersected volume in the mediolateral (ML), dorsoventral (DV) and anteroposterior (AP) axes, 3) to model the influence of CHPs size, shape and cell body placement inside the dendritic domain, on intersection, 4) to test whether results are replicable when examining natural pair intersection using the original placement of neurons inside the brain and, finally, 5) to test whether these methodologies are suitable to study intersection dynamics in other neuronal populations.

As shown below, we provide evidence that supports the convex hull assumption for dendritic shape and intersection and describe that pair to pair intersection dynamics are diverse and complex. We then go on to demonstrate a particularly important role of neurons CHP shape homogeneity in dendritic fields intersection. Finally, we report that this experimental approach can be used in other central neuronal populations exhibiting diverse sizes and morphologies, and that, regarding VTA DA neurons, intersection principles revealed by modeling are replicated when studying neurons in their original brain location.

115 # 2. MATERIAL AND METHODS

116 ## 2.1 Reconstructed neurons

117 Reconstructed DA neurons came from a pool of previously reported mouse neurons (VTA, n =
118 15; SNc, n = 15, (Farassat et al., 2019; Meza et al., 2018; Montero et al., 2021)). Briefly, neurons
119 were labeled with Neurobiotin using juxtacellular or intracellular labeling methods and brain
120 tissue was processed to reveal Neurobiotin and tyrosine hydroxylase to confirm the
121 dopaminergic profile. Next, neurons were manually reconstructed using Neurolucida (MBF
122 Bioscience) from confocal image stacks (more details in (Montero et al., 2021)). The
123 somatodendritic domain was completely filled, shrinkage corrected and reconstruction tilted-
124 corrected. For some analyses (Figure 2B, Figure 8), individual neuronal reconstructions were
125 placed in a custom-made 3D map of the VTA based on (Fu et al., 2012), according to the ML,
126 DV, and AP location of the cell body (Figure 8A).
127 Also, neurons from other studies were used from the neuromorpho.org database, which
128 fulfilled the following criteria: a) reconstructed from in vivo experiments such that no dendrites
129 are lost, b) somatodendritic domains were completely filled, c) shrinkage correction was
130 applied and d) orientation of neurons in relation to the cartesian space was known. The
131 following neurons were used: SNc DA neurons (rat, n = 10, (Henny et al., 2012)), cerebellum,
132 anterior lobule V of vermis (PC, mouse, n = 10, (Nedelescu et al., 2018)), mediodorsal thalamic
133 nucleus neurons (MD, rat, n = 5, (Kuramoto et al., 2017)) and spinal motoneurons (MN, rat, n =
134 3 (Rotterman et al., 2014)).

135

136

137 ## 2.2 Morphological analyses

138 Morphological and 3D wedge data were extracted using Neurolucida Explorer software (MBF
139 Bioscience). For wedge analysis, the distribution of the dendritic processes as they extend from
140 the cell body in every direction was obtained. To achieve this, the neuron is placed in the center
141 of a cylinder, which in this study was divided into 4 angular wedges, and in 2 parallel planes
142 perpendicular to the direction of the cylinder, with the division of the planes centered in the
143 cell body. For instance, if the cylinder is placed parallel to the anteroposterior axis, the four
144 angular wedges report the location of the processes in the dorsomedial, ventromedial,
145 ventrolateral, and dorsolateral quadrants, at each of the 2 planes defined in the AP axis (Figure
146 2A2, left). Results were presented as a percentage of the total dendritic length in each
147 quadrant. A similar procedure was used to analyze the wedge from CHPs (CHP wedge analysis,
148 Figure 2A2, right). This analysis was performed using a custom MATLAB (Mathworks) script. In
149 this case, the percentage of the total CHP volume was determined in each quadrant of the
150 anterior and posterior planes.

151 ## 2.3 Shape of CHP

152 To obtain the actual shape of CHP of an individual neuron, the *convhulln* function in MATLAB
153 was used. The *convhulln* function is based on Quickhull algorithm from Barber et al., 1996
154 (Barber et al., 1996), which allows the obtain the smallest CHP from a given set of points. The
155 input for the *convhulln* function was the *Segment points-dendrites* data from Neurolucida,
156 which contains the 3D coordinates of each dendritic segment. The outputs of *convhulln* are the

list of vertices that form a facet and the volume of the CHP. The volumes of CHPs obtained using *convhulln* coincided with the volumes reported for CH by Neurolucida Explorer (MBF Bioscience).

2.4 Intersected volume

Obtaining the volume of the intersected polyhedron required a transformation of the way the CHPs were encoded. For that, using MATLAB, we started from the original CHP and obtained the vertices. By using the *linspace* function, vertices forming each CHP facet were joined using 1000 points per CHP edge. Thus, we ended with a transformed CHP defined by points lined up along edges. To obtain the intersected polyhedron between pairs of CHPs, we proceeded as follows: using the *inhull* function (D'Errico, 2021), the points from each transformed CHP edge that are inside the other CHP of the pair were obtained, and then the *convhulln* function was used to obtain the intersected CHP and the intersected volume.

2.4.1 Intersection ratio

It was reasoned that because the intersected volume depends strongly on the volume of individual neurons CHPs (for instance, the intersected volume of two large but minimally intersected neurons could be the same as the intersected volume of two small but largely intersected neurons), it was necessary to find a ratio that normalized for the volume. As such, it was decided to work with an intersection ratio (IR), that is defined as follows:

$$Intersection\ Ratio = \frac{Intersected\ Volume}{Non\text{-}intersected\ Volume} x\ 100$$

$$Non\text{-}intersected\ Volume = CHP\ Volume\ 1 + CHP\ Volume\ 2 - Intersected\ Volume$$

175 We decided to normalize by the non-intersected volume, and not by the total added volume of
176 both individual neurons, so that the ratio approaches 100 for maximally overlapping CHPs. In
177 any event, the results in the vast majority of analyses did not vary between ratios using either
178 the *non-intersected volume* or the *total added volume* as divisors (not shown), nor when total
179 intersected volume was used.

180 2.4.2 Dendritic length and nearest neighbor inside intersected volume

181 First, using the *Segment points-dendrites* data from Neurolucida Explorer in MATLAB, each
182 neuron dendritic segment was resampled, in order that the distance between dendritic
183 segments were equal to 0.001 µm (new dendritic segments). Then, after determining the
184 intersected volume between pairs of CHPs, the *inhull* function was used to search which new
185 dendritic segments from each neuron where inside the intersected volume. Following, the
186 dendritic length inside the intersection (in µm) corresponded to: number of new dendritic
187 segments (inside the intersected CHP) x 0.001.
188 After determining which dendritic points were inside the intersected volume, the nearest
189 neighbors between the new dendritic segments of the pair of neurons were determined using
190 the *knnsearch* function. Then, the nearest neighbor from the pair of neurons was the minimum
191 value from the output matrix from *knnsearch*.

192 2.5 Methods of CHP geometry modeling

193 The following methods were developed using custom MATLAB scripts. For each of these
194 methods, IR was calculated at increasing distances between cell bodies (i.e., cell bodies of each
195 neuron, except for normalized cell body, see below), from 0 to 400 µm, at 10 µm steps. One

196 neuron of the pair was moved at these distances across the ML axis, then the DV axis, and
197 finally the AP axis.
198

199 ### 2.5.1 Normalized volume

200 Neurons CHPs were centered in the origin in relation to their cell body, and then the CHPs
201 vertices coordinates were multiplied by the following conversion factor:

$$\sqrt[3]{\frac{New\ CHP\ volume}{Original\ CHP\ volume}}$$

202 The converted CHPs conserve their shape and the position of their cell body.

203 ### 2.5.2 Normalized shape

204 To address the effect of CHP shape on IR, we needed first a rationale and then a method to
205 define an average CHP in 3D. The chosen rationale can be narrated as follows: let's imagine an
206 apex centered at 0, 0, 0 and from which rays emanate in all directions in space. Then the cell
207 bodies of a pair of CHPs are placed at the apex (as shown in Figure 4C, see also Supplementary
208 Figure 1). Any single ray will intersect the facets of the two CHPs at distances d1 and d2. Then, a
209 point at mid-distance between d1 and d2 is defined, and the exercise is repeated for all rays
210 emanating from the apex. A new polyhedron will be created by all points located at mid-
211 distance between the facets of both CHPs at every solid angle. This procedure can be projected
212 to a larger number of neurons CHP, in which case the points of the new polyhedron will
213 correspond to the average of all *n* distances at which rays intersect the facets of all CHPs in a
214 given ray direction.

215 Explained in detail, the procedure is based on a surface-to-point transformation procedure. It
216 starts by placing the cell body of a CHP on the center of a Cartesian space (0, 0, 0) where the
217 three orthogonal axes (ML, DV and AP) intersect. Then, a plane (e.g. AP – ML plane) orthogonal
218 to one axis (DV) is chosen, and the distances from the center to the CHP facets in that plane are
219 measured. This is repeated 360 times in 1-degree steps, in an anticlockwise direction. That
220 defines a polygon formed by 360 points (Supplementary Figure 1 A1-5). To move from that
221 polygon to a 3D polyhedron, the original plane is systematically tilted in 1-degree steps around
222 a new axis (e.g. the ML axis). That creates a polyhedron with 64800 points on its surface
223 (Supplementary Figure 1 A6-10). This process for the ML-DV plane, and for the AP-DV plane. To
224 obtain a CHP average from a given number of CHPs, the transformed CHPs were centered in the
225 origin, using the cell body as a reference point. Then, the mid-distance between analogous
226 points on the surface of their respective CHP was determined. A simplified 2D explanation for
227 the average process of 2 or 15 convex hull polygons is provided in Supplementary Figure 1 A
228 and B, respectively. It should be noticed that a consequence of this procedure is that the
229 resulting polyhedron (or resulting polygon in the simplified 2D explanation of Supplementary
230 Figure 1 A and B) is likely not to be convex all around its surface (Supplementary Figure 1 A), for
231 which an approximate convex hull must be defined using the *convhulln* function. On the other
232 hand, the more CHP are included, the more similar is the resulting polyhedron to its convex hull
233 (Supplementary Figure 1 B).

234 2.5.3 Normalized cell body position

235 First neurons CHPs were centered in the origin. Then, the centroid of each CHP was obtained
236 using the *centroid* function (Michael Kleder, 2022). Following, the CHPs were centered to the

237 origin subtracting the centroid coordinates to the corresponding vertices coordinates. With
238 these, the cell body of the neurons CHPs were changed to the centroid.
239
240

241 2.5.4 Average neuron according to isotropy index, morphology, and dendritic
242 distribution

243 The isotropy index was used to estimate how different from a sphere each CHP was. Each
244 neuron CHP was centered in the origin (coordinate 0,0,0), using the cell body as the reference
245 point. Then, a sphere, that had the same volume as the CHP, was also centered in the origin (in
246 relation to the sphere centroid). Following, the intersection volume was obtained. The isotropy
247 index correspond to the ratio between the intersected volume and the CHP volume. To obtain
248 the average isotropy index neuron, the median of isotropy index from the population was
249 calculated.
250 For the average morphology neuron, the following parameters obtained from Neurolucida
251 Explorer were used: dendritic length, dendritic tree number, maximum dendritic order, number
252 of segments and convex hull volume. For each parameter, the absolute deviation from the
253 mean was obtained (absolute value of the subtraction between each data and the mean of the
254 corresponding parameter). Then, for each neuron, the sum of the absolute deviations from the
255 mean was calculated. The neuron with lower value corresponded to the average morphology
256 neuron.

257 For average wedge neuron, the dendritic wedge data for the 4 anterior and 4 posterior
258 quadrants of each neuron was obtained. Then, the absolute deviation from the mean was
259 calculated for each quadrant. Following, for each neuron, the sum of the absolute deviations
260 from the mean was calculated. The neuron with lower value corresponded to the average
261 wedge neuron.
262
263

264 2.6 Computational and statistical analysis

265 MATLAB R2018a was used on a Lenovo P51 (Intel i7-7820HQ, 16 Gb of RAM, NVIDIA Quadro
266 M1200) with Windows 10. Statistical analyses were performed on MATLAB. Two-way ANOVA
267 was used (Figure 2A3). Spearman correlation was used for Figure 2A1, B3. Friedman test
268 followed by Dunn-Sidak post-test was used (Figure 8C). Wilcoxon rank sum test and signed rank
269 test, with Sidak multiple comparisons correction (*pval_adjust* function, (Fachada & C. Rosa,
270 2018)) were performed (Figures 6, 7, 8). An exponential decay model was used (Figure 8B).
271 Significance for all statistical tests was set at $p < 0.05$.
272

3. RESULTS

3.1 CHP volume and intersection between CHPs pairs: method and validation

In this work, we developed methods to determine the intersection between the dendritic domain of pairs of adjacent neurons and further studied how the distance between neuronal pairs, as well as the volume, shape and cell body position of each respective dendritic domain affects how much their domains intersect. For most of this work, we used a sample of 15 previously reconstructed VTA DA neurons (Figure 1B, original data from (Montero et al., 2021)). VTA DA neurons show a high overlap of their dendritic fields (Montero et al., 2021; Phillipson, 1979), making them a useful sample to test dendritic field intersection using CHPs.

A depiction of volume intersection between the dendritic domain of two neurons is shown in Figure 1. The two reconstructed VTA DA neurons were placed in their approximate position within the brain tegmentum (A, left, as shown in (Montero et al., 2021)). When considering the CHP derived from the disposition of dendrites in space (Figure 1, center), an intersected volume was defined (Figure 1, right, gray volume, more details in methods).

We started by validating the use of CHP as a proxy of the distribution of dendrites in space (Figure 2). First, the CHP volume showed a significant correlation with the dendritic length in our sample (Figure 2A1, $r = 0.7536$, $p = 0.0017$, Spearman correlation). To better understand this correlation, we checked whether the extension of dendrites (measured in length) in a space portion surrounding the cell body (Figure 2A2, left) was proportional to the CHP extension (measured in volume) in the same space portion (Figure 2A2, right). For that, we performed a

294 wedge analysis (see Methods), dividing the dendritic field of each neuron into 4 anterior and 4
295 posterior quadrants, as centered on the cell body, and determined the proportion of dendritic
296 length in each of these quadrants. We compared that to the proportion of CHP volume in each
297 respective quadrant (Figure 2A3) and found that there were no significant differences between
298 them (Two-way ANOVA Interaction: Anterior quadrants, $F_{(3,42)}$=0.4797 p=0.6981; Posterior
299 quadrants, $F_{(3,42)}$=0.6734 p=0.5732), thus validating the use of CHP as an adequate proxy for the
300 distribution of dendrites in space.
301 We then evaluated the proximity between dendrites of each neuron in the CHP intersection.
302 Figure 2B1 shows a representative pair of VTA DA neurons, located in their respective positions
303 in the VTA (Montero et al., 2021), with their corresponding neuronal CHPs and the CHP
304 intersection (gray). It can be observed that both neurons showed dendrites inside the CHP
305 intersection. Relevantly, the distance between the nearest neighbor segments was 17 µm.
306 When this was assessed for all the VTA DA neuronal pairs in their respective position in the VTA
307 (more details about this in Figure 8 and in methods), a left-skewed distribution was observed,
308 with a median value of 4.6 µm (Figure 2B2, n = 64 pairs with an IR>0), indicating that inside the
309 CHP intersection dendrites are close to each other.
310 We found that for 84% of the pairs, nearest neighbor distances lower than 25 µm were
311 observed. Moreover, a significant correlation between the intersection volume and the
312 dendritic length inside the intersection was found (Figure 2B3, r = 0.9685, p < 0.001, Spearman
313 correlation). Overall, these results show that the intersection of neurons CHPs is a
314 representative proxy of the intersection between dendritic fields.
315

316 ## 3.2 CHP intersection dynamics: modeling the influence of CHP volume,
317 shape and cell body position

318 Following method validation, we evaluated how the intersection between pairs of neurons
319 CHPs changes when the distance between CHPs increases (Figure 3A). We used an intersected
320 ratio (IR, more details in methods) as a normalized index of intersection between pairs of
321 neurons CHPs. Then, IR values were obtained from pairs of VTA DA neurons, first with their cell
322 bodies aligned (distance between cell bodies = 0 µm) and then after one of the neuron CHP was
323 moved across the ML, DV or AP axes (in 10 µm steps, until 400 µm). In Figure 3B we show some
324 representative examples of IR vs distance curves. We found a high variability in IR as a function
325 of distance. For instance, in Figure 3B (ML), the green curve shows a pair of CHPs whose IRs first
326 increased, then reached a peak, and then decreased, in contrast to the magenta and red curves,
327 whose IR values only decreased. These results indicate that IR between neuronal pairs depends
328 on the distance between their cell bodies, but also on other geometrical factors.
329 To understand how the differences in geometry between neuronal pairs affect intersection, we
330 separately modeled the influence of neurons CHP volume, shape, and cell body position (Figure
331 4, see methods) by running the same previous simulations (as in Figure 3), but this time with all
332 pairs having either a normalized volume, a normalized shape or a normalized cell body position.
333 More precisely, we first transformed all CHPs to a normalized volume, which was equal to the
334 population mean for VTA DA neurons (0.047 mm^3). In Figure 4A,B we show a simpler
335 description of the procedure using only two neurons CHPs. Their respective volumes are 0.069
336 mm^3 and 0.023 mm^3 (Figure 4A), therefore one of them decreases its volume to the average

337 value (Figure 4B, neuron CHP 14), and the other increases its volume to the average value
338 (Figure 4B, neuron CHP 3). Note that the CHP shape remains unchanged with this procedure.
339 To examine the effect of differences in CHP shape on IR we reasoned that, similarly, this could
340 be assessed using a normalized shape from the population of CHPs. We set to find a CHP that
341 we defined as the CHP of the polyhedron formed by the points located at average distances
342 from the surfaces of all CHP, with their cell bodies aligned. After the normalized CHP is defined,
343 its volume can be modified to the volume values of the original neurons CHPs. In Figure 4C we
344 show a simpler description of the procedure using only two neurons CHPs. The CHPs of the
345 previous pair now were combined to generate a normalized shape following the averaging rules
346 already explained (Figure 4C, top row, more details in Supplementary Figure 1 and methods).
347 Then, the new normalized CHP was given back the original CHP volumes (Figure 4C, bottom
348 row).
349 The normalized shape of all VTA DA neurons is shown in Figure 5A. As it can be appreciated, the
350 average shape exhibits the essential geometrical features of this dopaminergic population,
351 particularly the dendritic domain size and the extension in the ML, DV and AP axes. In frontal
352 view, we observe that the CHP was oriented dorsomedially to ventrolaterally, with the cell body
353 at mid position, in agreement with the distribution of VTA neurons dendritic field, as described
354 in (Montero et al., 2021).
355 Finally, we took into account the fact that, as it can be noted in Figure 1B, the cell bodies of real
356 VTA DA neurons are normally displaced from the center of the dendritic domain. We
357 considered this a relevant factor for intersection and therefore defined a third normalization
358 procedure, in which the cell body of each CHP was moved to the CHP' centroid. Again, in Figure

359 4D we show a simpler description of the procedure using only two neurons CHPs (more details
360 in methods).
361 We applied the modeling procedures described above to our population of VTA DA neurons
362 (Figure 6). In each condition and in the ML, DV or AP axes, all the possible pairs of VTA DA
363 neurons were analyzed (210 pairs in total, using repeating pairs given that a neuron "a" in a pair
364 is first tested moving away from neuron "b", and then neuron "b" is tested moving away from
365 neuron "a"). Compared to the original data (no changes in CHP geometry), a significant increase
366 in IR was found in the normalized volume condition across the ML (Figure 6A1), DV (Figure 6A2)
367 and AP (Figure 6A3) axes ($p < 0.05$ using Wilcoxon signed rank test with Sidak multiple
368 comparisons correction, more details of statistical differences between conditions in Figure 6A),
369 but the magnitude of change in IR was low. For the normalized cell body position condition,
370 significantly higher IR values were observed in the three axes, compared to the original data
371 and also to the normalized volume condition (Figure 6A1-3). However, the modeling condition
372 that showed the largest effect on IR values across each axis, was the normalized shape
373 condition (Figure 6A1-3). These results indicate that differences in IR values between pairs of
374 VTA DA neurons CHPs are influenced, in decreasing order, by the CHP shape, cell body position,
375 and volume.
376 To give further sustain to the results describing the influence of shape normalization on
377 intersection (see discussion), we used CHPs from neurons that exhibited average values for
378 morphology, isotropy and dendritic distribution characteristics, as follow: 1. average isotropy
379 neuron: for each neuron CHP, an isotropy index was calculated to determine how much a CHP
380 is similar to a sphere of the same volume (more details in methods); then the median

381 population value was found (0.46), and the neuron with the closest value was selected (in this
382 case neuron 7 (Figure 1B)); 2. average morphology neuron: using the dendritic length, dendritic
383 tree number, maximum dendritic order, number of segments and convex hull volume, we
384 found the neuron with the lower absolute deviation of the mean from the sample (more details
385 in methods), which corresponded to neuron 14 (Figure 1B); 3. average dendritic distribution
386 neuron: using the dendritic wedge data for the 4 anterior and 4 posterior quadrants (Figure
387 2A3), we found the neuron with the lower absolute deviation from the mean from the sample
388 (more details in methods), which corresponded to neuron 1 (Figure 1B). Each average neuron
389 was then analyzed using the same approach as for the normalized shape analysis: starting with
390 one of the three average neurons, we created 15 new CHPs, all with the average neuron CHP
391 shape, and then gave to each new CHP the respective 15 volumes from the VTA DA neurons
392 population. And then determining IR values between 0 to 400 µm (10 µm steps) across the ML,
393 DV and AP axes.
394 Figure 6B shows the IR curves for average isotropy neuron, average morphology neuron and
395 average dendritic domain neuron. Each condition was compared with the original data analysis
396 across each axis. All three average neurons showed significantly higher IR values than the
397 original condition ($p < 0.05$ using Wilcoxon signed rank test with Sidak multiple comparisons
398 correction, more details of statistical differences between groups in Figure 6B) and almost
399 identical magnitudes to that of CHP shape normalization in 6A.
400 We wanted to further examine the diversity of distance versus IR curves shown previously
401 (Figure 3), this time focusing on the types of decay curves observed. For the original data, we
402 found that 51% of the curves for all pairs and axes tested, described an initial decay ("decay

403 curves", as the magenta or red curves in Figure 3B, ML), whereas 49% of curves exhibited an
404 initial rise, a peak, and then a decay ("peak curves", as the green curve in Figure 3B, ML). After
405 volume normalization, the proportion of decay and peak curves remained similar to the original
406 data (51% vs 49%). Interestingly, in the normalized cell body condition, an increase in decay
407 curves cases was observed (57%, versus 43% of peak curves). Yet the larger effect was found in
408 the shape normalization condition, where peak curves disappeared and thus 100% of the
409 curves ended as decay curves. Overall, these results are in line with the previous findings of this
410 section, highlighting that CHP shape is the main factor that contributes to the variability in
411 intersection dynamics.

412 3.3 CHP intersection dynamics: examples from other neuronal types

413 To further characterize our proposed method to study intersection of dendritic fields, we
414 searched for in vivo labeled neurons in the neuromorpho.org database (more details in
415 methods). The following pools of neurons were used: cerebellar Purkinje neurons (PC, n= 10,
416 (Nedelescu et al., 2018)), substantia nigra pars compacta (SNc) DA neurons from rat (n = 10,
417 (Henny et al., 2012)) and mouse (n = 15, (Farassat et al., 2019; Meza et al., 2018; Montero et al.,
418 2021)), medio dorsal thalamic neurons (MD, n = 5, (Kuramoto et al., 2017)) and spinal
419 motoneurons (MN, n = 3, (Rotterman et al., 2014)). Figure 5B shows the normalized shape of
420 these neuronal populations.

421 We first computed the IR dynamics of the neuronal CHPs (original data) of each region, and
422 qualitatively examined differences between cell types (Figure 7A). MN neurons show higher IR
423 values in the three axes, followed by MD, SNc rat and mouse neurons, and PC cells, although
424 each population shows specific differences in each axis.

425 As with VTA neurons (Figure 6), we modeled CHP geometry for PC, SNc, MD and MN neurons
426 populations, using the normalized volume, normalized shape and normalized cell body position
427 conditions (Figure 7B). We show the most representative axis of each neuronal population. As
428 in the original condition analysis (Figure 7A), mouse and rat DA neurons showed similar curve
429 profiles after the application of each modeling conditions in the ML axis (Figure 7B1-2).
430 Specifically, in both SNc mouse (Figure 7B1) and rat (Figure 7B2) analysis, normalized volume
431 showed increased IR values than the original condition ($p < 0.05$, Wilcoxon signed rank test with
432 Sidak multiple comparisons correction, more details of statistical differences between
433 conditions in Figure 7B1-2), but the magnitude of change in IR is low. The normalized cell body
434 location modeling also showed significantly higher values than the original and also the
435 normalized volume conditions in both SNc mouse and rat neurons, but the magnitude of
436 change was higher in SNc rat. The largest effect for both mouse and rat SNc DA neurons was
437 observed in the normalized shape condition, which was significantly higher than the other three
438 conditions. These results were very similar to those found with VTA DA neurons (Figure 6A),
439 indicating a common underlying dendritic organization.
440 Interestingly, modeling conditions applied on MD neurons only significantly modified IR values
441 on short distances on the ML axis ($p < 0.05$, Wilcoxon signed rank test with Sidak multiple
442 comparisons correction, more details of statistical differences between conditions in Figure
443 7B3). These results indicate that neither volume, shape or position of the cell body is relevant
444 to explain the intersection dynamics in MD neurons.
445 For MN, no significant differences were observed between conditions, although normalized
446 shape showed a trend of higher values than the other conditions (Figure 7B4). The lack of

447 significant differences could be related to the low sample of neurons in this region (3 neurons,
448 6 pairs analyzed at each distance).
449 Finally, for PC, we first show the ML axis as a positive control for our results, considering the
450 mainly 2D structure of the PC dendritic field, and minimal extension in the ML axis. In this
451 sense, the modeling conditions only showed an effect at a distance between cell bodies of 0
452 µm, with a fast decrease of IR values at 10 µm (Figure 7B5'). A different result was found at the
453 AP axis (Figure 7B5''), a more biologically relevant condition, considering the default sagittal
454 arrangement of these neurons in the cerebellum. A significant difference between the original
455 and normalized volume condition was observed, but the magnitude of the difference was low
456 ($p < 0.05$, Wilcoxon signed rank test with Sidak multiple comparisons correction, more details of
457 statistical differences between conditions in Figure 7B5''). Higher IR values were found after
458 normalizing cell body location and shape, until 50 µm. In summary, these results indicate that
459 intersection dynamics appear to be cell-type specific.

460 3.4 CHP intersection dynamics using neurons real position in the VTA

461 As a final approach to characterize the uses of the CHP intersection method for neurons, we
462 again used our sample of VTA DA neurons, but now to analyze IR dynamics using the real
463 positions of the neurons in the region (as determined in (Montero et al., 2021)). As seen in
464 Figure 8A, our sample of DA neurons is located in the central region of the VTA (see Discussion).
465 IR values for all the possible pairs were obtained (105, without repeating). This analysis was
466 performed for the original data (Figure 8B1), and the three modeling conditions used in the
467 previous sections: normalized volume (Figure 8B2), normalized shape (Figure 8B3), and
468 normalized cell body location (Figure 8B4). For the original data, high variability in IR values

469 across distance was found (Figure 8B1), as data show a low R^2 for an exponential decay non-
470 linear regression (R^2 = 0.4231). A similar IR profile was found in the normalized volume
471 condition (Figure 8B2), confirming a low effect of volume variability in intersection dynamics (as
472 also found in Figure 6A), with an even lowest R^2 for an exponential decay fit (R^2 = 0.3232).
473 Interestingly, shape and cell body location normalization drastically changed the data curve
474 profile and reduced the variability of IR values across distances (Figure 8B3-4), as evidenced by
475 a higher exponential decay fit (normalized shape: R^2 = 0.8373; normalized cell body: R^2 =
476 0.7595). Finally, we analyzed the IR values of the closer 50% (0 to 340 µm, n = 53 pairs, Figure
477 8C1) and farther 50% (340 to 807 µm, n = 52 pairs, Figure 8C2) of distances between cell
478 bodies. For the closer half of distances (Figure 8C1), we found significantly higher IR values in
479 the normalized shape conditions compared to the original data ($p < 0.001$, Friedman test
480 followed by a Dunn's multiple comparisons test). On the other hand, for larger distances (Figure
481 8C2), original and normalized volume conditions were significantly higher than both normalized
482 shape and cell body conditions (details in Figure 8C2).
483 Overall, the results using real neurons positions in the VTA confirm the principles described in
484 Figure 6: CHP shape, and to some extent cell body location, in VTA DA neurons are the most
485 relevant factors underlying CHP intersection between pairs of VTA DA neurons.
486

4. DISCUSSION

4.1 Use of CHPs to study dendritic domain intersection

CHPs have been used to characterize and classify neuronal populations shape or size (Felix et al., 2013; Gärtner et al., 2004; Gertler et al., 2008; Ito, 2020; Kawa et al., 1998; Malmierca et al., 1995; Mihaljević et al., 2015; Rojo et al., 2016). We adapted previously developed computational tools to determine intersected volume between pairs of polyhedrons (Chazelle & Dobkin, 1987; Govender et al., 2018; Muller & Preparata, 1978) to explore in greater detail the effects of various 3D geometrical factors on CHPs intersection, at the single cell level.

The use of neurons' CHPs to represent dendritic domain size or shape (Felix et al., 2013; Gärtner et al., 2004; Gertler et al., 2008; Ito, 2020; Kawa et al., 1998; Malmierca et al., 1995; Mihaljević et al., 2015; Rojo et al., 2016) poses the question of the extent to which the CHP is indeed an appropriate proxy, given that the vast majority of space within a neuronal CHP is not occupied by dendritic segments. And, similarly, whether intersection between CHPs reflects dendritic domain intersection in any biologically meaningful way. We examined the shape assumption by testing whether CHP and dendritic length space distribution were comparable. We first confirmed that larger CHP does indeed contain more dendritic length (Figure 2A1). Then we examined the spatial distribution of CHP volume and dendritic length and found that they were indistinguishable from each other, as tested using wedge analysis in Figure 2A3. These results support the contention that CHPs are adequate proxies for dendritic distribution.

We then tested the CHP intersection assumption by studying the proximity between the dendrites from two neurons located inside the intersected volume. We found that the median

508 nearest neighbor distance between dendrites from different neurons inside the intersected
509 volume was 4.6 µm, and that in almost 85% of the cases, at least one pair of dendrites located
510 at less than 25 µm (Figure 2B2). To put these results in perspective, a 25 µm distance is similar
511 to the longest axis of DA neurons cell bodies (see Figure 1 in (Meza et al., 2018; Montero et al.,
512 2021)). Finally, we determined that the total length of shared dendrites inside the intersected
513 volume tightly correlates with the CHPs intersected volume (Figure 2B3). These data support
514 the assumption that CHP intersection is an appropriate proxy for the intersection of neuronal
515 dendritic fields.
516 Having confirmed these assumptions, it is important to stress, however, that CHP does not
517 represent and are therefore not useful to describe other aspects of dendritic organization, such
518 as dendritic density or architectural complexity inside the CHP, as CHPs only considers the outer
519 limits of a dendritic domain. Thus, other systematic modeling approaches must be used if one
520 wants to study the influence of dendritic density or architecture on intersection. We consider
521 those possible approaches, which we imagine would require combining methods that model
522 dendritic architecture (Ascoli & Krichmar, 2000; Cuntz et al., 2010, 2012; Takeo et al., 2021)
523 with those developed here to model distance and compute the intersection, of utmost
524 importance and would certainly complement and illuminate the results described in the
525 present study.

526 4.2 Normalized and representative CHPs

527 In order to study the influence of shape on intersection, an additional challenge in this study
528 was to find a CHP whose shape best represented an otherwise diverse population. We took the
529 direct, though methodologically more challenging approach, to compute the average 3D CHP

530 shape from the population of 15 neurons CHPs. This approach allowed us to model intersection
531 using a normalized shape, while maintaining the original volume and cell body position of CHPs.
532 Now, because the resulting average CHP is smooth and ovoid-shaped, one reasonable concern
533 is that the observed increases in intersection are merely due to these characteristics, and not
534 due to the use of a normalized shape To address this issue, we chose three CHPs whose
535 respective neurons exhibited average morphology (Montero et al., 2021), isotropy (see
536 methods), and spatial dendritic distribution (Figure 2A3 and methods). In this way, we could
537 use CHPs with average characteristics, but whose CHP maintained its pointed, original shape,
538 thus discarding an artificial influence from the smother, ovoid-shaped average CHP.

539 4.3 Role of distance, volume, cell body location and shape on 540 intersection

541 Our results show that in addition to cell-to-cell distance predictably decreasing intersection,
542 distance versus intersection relationship was not straightforward and had to depend on other
543 geometrical factors. Indeed, intersection was affected by the relative position of each neuron to
544 its pair (i.e. whether one locates besides, above/below, or in front/behind from the other). This
545 is an expected consequence of the dendritic domain of neurons not being spherical (i.e. in that
546 maximal extensions in ML, DV or AP axes differ from each other). The location of the cell body,
547 which we used to identify each neuron and showed displacement from the dendritic domain's
548 centroid, was also a relevant factor influencing intersection dynamics. Yet perhaps the most
549 noteworthy finding of this study, however, is that dendritic domain intersection is significantly
550 increased by shape homogeneity between neurons (Figure 6-8). Or, said conversely, that

551 dendritic domain exclusion between adjacent neurons is significantly increased by
552 heterogeneity in dendritic domain size and shape.
553 We found that individual pairs distance vs intersection decay dynamics were diverse. Among
554 them, some curves exhibited a peak, i.e., an initial rise followed by the expected decay. We
555 found this result interesting because it challenges the intuitive assumption that neurons whose
556 cell bodies locate next to each other should have a maximal chance of sharing afferents inputs.
557 We initially assumed that this specific dynamic (peak curves) mostly resulted from the displaced
558 location of the cell bodies within their respective CHP, resulting in dendritic domains sharing
559 little volume with their cell bodies aligned (for instance, in a hypothetical scenario in which two
560 Purkinje-like cells had their cell bodies aligned, but their respective dendritic domains pointing
561 in opposite directions). Interestingly, however, although cell body position normalization
562 diminished the proportion of peak curves, shape normalization completely eliminated them,
563 again emphasizing the critical role of CHP shape in determining intersection dynamics.

564 4.4 Determinants of VTA DA neurons morphology and overlap

565 The principles that underlie intersection ultimately depend on the size and spatial organization
566 of VTA DA dendrites. As detailed in (Montero et al., 2021), the dendritic tree of individual
567 mouse VTA DA neurons conforms to early descriptions (Kline & Felten, 1985; Phillipson, 1979;
568 Ramón-Moliner & Nauta, 1966) characterizing them by long radiating dendrites, low branching
569 patterns, and overall conforming to the "isodendritic" cell type typical of reticular neurons
570 (Jones, 1995; Ramón-Moliner & Nauta, 1966).
571 The mechanisms involved in specification of VTA neurons dendritic trees have not been studied
572 in detail yet (Brignani & Pasterkamp, 2017). We speculate that dendritic morphogenesis of VTA

573 DA neurons is likely to rely on the catenin signaling pathway, which plays a critical role in VTA
574 DA neurons neurogenesis and migration (Tang et al., 2009) and, as studied in other brain
575 regions, is essential for dendritic growth and branching (Arikkath, 2009). On the other hand,
576 given the highly overlapping pattern of VTA DA neurons dendritic trees, there must also exist
577 mechanisms that allow the co-existence of dendrites from neighboring cells that belong to the
578 same cell class (dopaminergic). Indeed, in the retina the dendritic domain of neighboring
579 amacrine dopaminergic (and other amacrine) cells overlap extensively. The mechanisms that
580 ultimately instruct or permit dendritic overlap are less known, although evidence points to the
581 self/non-self discrimination capacity of developing neurons which on the one hand, avoid
582 aberrant branching towards themselves, but on the other, permits growing towards other
583 same-class neurons. Interestingly, this is a process mediated by protocadherins (Lefebvre, 2017;
584 Lefebvre et al., 2015), a group of cell adhesion molecules that are also expressed in the VTA
585 (Hertel et al., 2008).

586 4.5 VTA DA neurons orientation and VTA region shape

587 Brain regions may exhibit structural folding, and therefore same class neurons may exhibit
588 dissimilar orientations. A pertinent question to ask is whether our sampled VTA DA neurons
589 may exhibit different orientations, perhaps related to the natural folding of the VTA, which may
590 have affected the intersection dynamics described here. As seen in the wedge analysis of
591 dendritic length spatial distribution in Figure 2, our neuronal sample exhibited a dorsomedial to
592 ventrolateral preferred orientation, something also evident in the overall orientation of CHPs in
593 Figure 1, and also in the depiction of neurons within the VTA in Figure 8. Therefore, we think
594 that modeling intersection in this sample is attainable. Indeed, the preferred orientation of VTA

595 DA neurons coincides with the orientation of the VTA nuclei in which these neurons locate,
596 which corresponds to the main parabrachial pigmented (PBP) and underlying paranigral and
597 parainterfasciular (PN/PIF) nuclei (Montero et al., 2021) all of which exhibit a dorsomedial to
598 ventrolateral orientation (Brignani & Pasterkamp, 2017; Fu et al., 2012; Montero et al., 2021),
599 and locate between the VTA midline nuclei (which exhibit a vertical orientation), and the lateral
600 wing of the PBP (which exhibit a dorsolateral to ventromedial orientation). Interestingly, the
601 orientation of VTA DA neurons and VTA nuclei described also coincides with the orientation of
602 migrating dopaminergic neurons precursors exhibit during the final stages of the ventral
603 midbrain development, indicating that the adult dendritic tree retained the orientation that
604 neurites present during development (Bodea et al., 2014; Brignani & Pasterkamp, 2017;
605 Kawano et al., 1995).
606 Finally, the similar orientation between VTA DA neurons dendritic domain and the VTA may
607 also explain why our modeling approach applied to neurons in their real brain coordinates
608 (Figure 8) showing that, again, similarity in shape was the most predominant factor increasing
609 intersection in their original positions.

610 4.6 Use of normalized CHV to study intersection dynamics in other 611 neuronal groups

612 We use normalized CHPs to understand intersection dynamics in neurons that present dendritic
613 domain size, shape, and cell body location that differ from our VTA DA neurons. We included
614 mouse and rat SNc neurons, which we have described and show a similar architecture to VTA
615 DA neurons (Henny et al., 2012; Montero et al., 2021), spinal motoneurons which are known to

616 exhibit a very large and dense dendritic tree (Rotterman et al., 2014) and described as
617 isodendritic (Ramón-Moliner & Nauta, 1966), and mediodorsal thalamic nucleus (Kuramoto et
618 al., 2017), which exhibit much smaller dendritic domains. We show that intersection dynamics
619 differ between cell types (Figure 7), for instance with a much less preponderant role of shape in
620 MD and motoneurons. And we also show similar dynamics for both rat and mouse SNc DA
621 neurons. We also include Purkinje cells (Nedelescu et al., 2018), which are characterized by
622 extremely displaced cell bodies and a two-dimensionally arranged dendritic domain that
623 generally does not overlap with neighboring neurons. In the context of this analysis, Purkinje
624 cells work as a positive control for the method because, as expected from its sagittally
625 organized two-dimensional dendritic domain, intersection in the ML axis falls rapidly.

626 **4.7 Perspective**

627 The broad spectrum of dendritic domain arrangements among neuronal types has been
628 conceptualized as representing different types of connectivity, either of the selective, sampling,
629 or space filling type (Harris & Spacek, 2017). The former type is characterized by small dendritic
630 fields occupying a restricted locus, and represents an efficient solution to relay nervous signals
631 from one neuronal stage to another as parallel, separate channels. The sampling strategy (and
632 to some extent the space filling's) connectivity strategy, on the other hand, is characterized by
633 broader dendritic fields encompassing different loci, and represents a solution to increase
634 integration and redundancy in signal transferring (Harris & Spacek, 2017). Our results allow us
635 to predict that, for a given number of neurons and a given dendritic length, systems that
636 require parallel and exclusive transferring of nervous signals may accomplish it by promoting
637 heterogeneity in size, cell body location and specially shape of dendritic domains. Conversely,

638 systems that require signal integration and redundancy may accomplish it by promoting
639 uniformity in dendritic domain size, cell body location and shape.
640

ACKNOWLEDGMENTS

We thank Luciana López-Juri for her insightful comments during the progress of this work. This work was supported by Fondo Nacional de Desarrollo Científico y Tecnológico Regular grants 1141170 and 1191497 to PH, and Comisión Nacional de Investigación Científica y Tecnológica REDES grant 180207 to PH.

DATA AVAILABILITY STATMENT

Raw data, MATLAB scripts and data analysis are available at https://github.com/hennylab/Neuronal-Convex-hull-intersection and we have archived our code on Zenodo https://doi.org/10.5281/zenodo.6941258. SNc and VTA neurons reconstructions are available at https://www.neuromorpho.org.

References

Arikkath, J. (2009). Regulation of dendrite and spine morphogenesis and plasticity by catenins. In *Molecular Neurobiology* (Vol. 40, Issue 1, pp. 46–54). Humana Press Inc. https://doi.org/10.1007/s12035-009-8068-x

Ascoli, G. A., & Krichmar, J. L. (2000). L-neuron: A modeling tool for the efficient generation and parsimonious description of dendritic morphology. *Neurocomputing*, *32–33*, 1003–1011. https://doi.org/https://doi.org/10.1016/S0925-2312(00)00272-1

Barber, C. B., Dobkin, D. P., & Huhdanpaa, H. (1996). The Quickhull Algorithm for Convex Hulls. *ACM Transactions on Mathematical Software*, *22*(4), 469–483. https://doi.org/10.1145/235815.235821

Bodea, G. O., Spille, J. H., Abe, P., Andersson, A. S., Acker-Palmer, A., Stumm, R., Kubitscheck, U., & Blaess, S. (2014). Reelin and CXCL12 regulate distinct migratory behaviors during the development of the dopaminergic system. *Development (Cambridge)*, *141*(3), 661–673. https://doi.org/10.1242/dev.099937

Braitenberg, V., & Schüz, A. (1998). *Cortex: Statistics and Geometry of Neuronal Connectivity*. Springer Berlin Heidelberg. https://doi.org/10.1007/978-3-662-03733-1

Brignani, S., & Pasterkamp, R. J. (2017). Neuronal subset-specific migration and axonal wiring mechanisms in the developing midbrain dopamine system. In *Frontiers in Neuroanatomy* (Vol. 11). Frontiers Media S.A. https://doi.org/10.3389/fnana.2017.00055

Brombas, A., Kalita-De Croft, S., Cooper-Williams, E. J., & Williams, S. R. (2017). Dendro-dendritic cholinergic excitation controls dendritic spike initiation in retinal ganglion cells. *Nature Communications*, *8*, 1–14. https://doi.org/10.1038/ncomms15683

Chazelle, B., & Dobkin, D. P. (1987). Intersection of convex objects in two and three dimensions. *Journal of the ACM (JACM)*, *34*(1), 1–27. https://doi.org/10.1145/7531.24036

Cuntz, H., Forstner, F., Borst, A., & Häusser, M. (2010). One rule to grow them all: A general theory of neuronal branching and its practical application. *PLoS Computational Biology*, *6*(8). https://doi.org/10.1371/journal.pcbi.1000877

Cuntz, H., Mathy, A., & Häusser, M. (2012). A scaling law derived from optimal dendritic wiring. *Proceedings of the National Academy of Sciences of the United States of America*, *109*(27), 11014–11018. https://doi.org/10.1073/pnas.1200430109

D'Errico, J. (2021). *Inhull*. https://www.mathworks.com/matlabcentral/fileexchange/10226-inhull

Fachada, N., & C. Rosa, A. (2018). micompm: A MATLAB/Octave toolbox for multivariate independent comparison of observations. *Journal of Open Source Software*, *3*(23), 430. https://doi.org/10.21105/joss.00430

Farajian, R., Raven, M. A., Cusato, K., & Reese, B. E. (2004). Cellular positioning and dendritic field size of cholinergic amacrine cells are impervious to early ablation of neighboring cells in the mouse retina. *Visual Neuroscience*, *21*(1), 13–22. https://doi.org/10.1017/S0952523804041021

Farassat, N., Costa, K. M., Stojanovic, S., Albert, S., Kovacheva, L., Shin, J., Egger, R., Somayaji, M., Duvarci, S., Schneider, G., & Roeper, J. (2019). In vivo functional diversity of midbrain dopamine neurons within identified axonal projections. *ELife*, *8*. https://doi.org/10.7554/eLife.48408

Felix, R. A., Vonderschen, K., Berrebi, A. S., & Magnusson, A. K. (2013). Development of on-off spiking in superior paraolivary nucleus neurons of the mouse. *Journal of Neurophysiology*, *109*(11), 2691–2704. https://doi.org/10.1152/jn.01041.2012

Fu, Y. H., Yuan, Y., Halliday, G., Rusznák, Z., Watson, C., & Paxinos, G. (2012). A cytoarchitectonic and chemoarchitectonic analysis of the dopamine cell groups in the substantia nigra, ventral tegmental area, and retrorubral field in the mouse. *Brain Structure and Function*, *217*(2), 591–612. https://doi.org/10.1007/s00429-011-0349-2

Gärtner, U., Alpár, A., Reimann, F., Seeger, G., Heumann, R., & Arendt, T. (2004). Constitutive Ras activity induces hippocampal hypertrophy and remodeling of pyramidal neurons in synRas mice. *Journal of Neuroscience Research*, *77*(5), 630–641. https://doi.org/10.1002/jnr.20194

Geisler, S., & Zahm, D. S. (2005). Afferents of the ventral tegmental area in the rat-anatomical substratum for integrative functions. *Journal of Comparative Neurology*, *490*(3), 270–294. https://doi.org/10.1002/cne.20668

Gertler, T. S., Chan, C. S., & Surmeier, D. J. (2008). Dichotomous anatomical properties of adult striatal medium spiny neurons. *Journal of Neuroscience*, *28*(43), 10814–10824. https://doi.org/10.1523/JNEUROSCI.2660-08.2008

Govender, N., Rajamani, R., Wilke, D. N., Wu, C. Y., Khinast, J., & Glasser, B. J. (2018). Effect of particle shape in grinding mills using a GPU based DEM code. *Minerals Engineering*, *129*(September), 71–84. https://doi.org/10.1016/j.mineng.2018.09.019

715 Groves, P. M., & Linder, J. C. (1983). Dendro-dendritic synapses in substantia nigra: Descriptions
716 based on analysis of serial sections. *Experimental Brain Research*, *49*(2), 209–217.
717 https://doi.org/10.1007/BF00238581
718 Harris, K. M., & Spacek, J. (2017). *Chapter 1: Dendrite structure; in Dendrites* (G. Stuart, N.
719 Spruston, & M. Häusser, Eds.; 3th ed.). OUP Oxford.
720 Henny, P., Brown, M. T. C., Northrop, A., Faunes, M., Ungless, M. a, Magill, P. J., & Bolam, J. P.
721 (2012). Structural correlates of heterogeneous in vivo activity of midbrain dopaminergic
722 neurons. *Nature Neuroscience*, *15*(4), 613–619. https://doi.org/10.1038/nn.3048
723 Herculano-Houzel, S. (2011). Not All Brains Are Made the Same: New Views on Brain Scaling in
724 Evolution. *Brain Behavior and Evolution*, *78*(1), 22–36. https://doi.org/10.1159/000327318
725 Hertel, N., Krishna-K, Nuernberger, M., & Redies, C. (2008). A cadherin-based code for the
726 divisions of the mouse basal ganglia. *Journal of Comparative Neurology*, *508*(4), 511–528.
727 https://doi.org/10.1002/cne.21696
728 Hinds, J. W. (1970). Reciprocal and serial dendrodendritic synapses in the glomerular layer of
729 the rat olfactory bulb. *Brain Research*, *17*(3), 530–534. https://doi.org/10.1016/0006-
730 8993(70)90263-5
731 Ito, T. (2020). Different coding strategy of sound information between GABAergic and
732 glutamatergic neurons in the auditory midbrain. *Journal of Physiology*, *598*(5), 1039–1072.
733 https://doi.org/10.1113/JP279296
734 Jan, Y. N., & Jan, L. Y. (2010). Branching out: Mechanisms of dendritic arborization. *Nature*
735 *Reviews Neuroscience*, *11*(5), 316–328. https://doi.org/10.1038/nrn2836

Jones, B. (1995). Reticular Formation: Cytoarchitecture, Transmitters, and Projections. In G. Paxinos (Ed.), *The Rat Nervous System* (2nd ed., pp. 115–171). Academic Press.

Kawa, A., Stahlhut, M., Berezin, A., Bock, E., & Berezin, V. (1998). A simple procedure for morphometric analysis of processes and growth cones of neurons in culture using parameters derived from the contour and convex hull of the object. *Journal of Neuroscience Methods*, *79*(1), 53–64. https://doi.org/10.1016/S0165-0270(97)00165-9

Kawano, H., Ohyama, K., Kawamura, K., & Nagatsu, I. (1995). Migration of dopaminergic neurons in the embryonic mesencephalon of mice. *Developmental Brain Research*, *86*(1), 101–113. https://doi.org/https://doi.org/10.1016/0165-3806(95)00018-9

Keeley, P. W., & Reese, B. E. (2010). Morphology of dopaminergic amacrine cells in the mouse retina: Independence from homotypic interactions. *Journal of Comparative Neurology*, *518*(8), 1220–1231. https://doi.org/10.1002/cne.22270

Kline, S., & Felten, D. L. (1985). Ventral tegmental area of the rabbit brain: a developmental Golgi study. *Brain Research Bulletin*, *14*(5), 485–492. https://doi.org/https://doi.org/10.1016/0361-9230(85)90027-9

Kuramoto, E., Pan, S., Furuta, T., Tanaka, Y. R., Iwai, H., Yamanaka, A., Ohno, S., Kaneko, T., Goto, T., & Hioki, H. (2017). Individual mediodorsal thalamic neurons project to multiple areas of the rat prefrontal cortex: A single neuron-tracing study using virus vectors. *Journal of Comparative Neurology*, *525*(1), 166–185. https://doi.org/10.1002/cne.24054

Lefebvre, J. L. (2017). Neuronal territory formation by the atypical cadherins and clustered protocadherins. In *Seminars in Cell and Developmental Biology* (Vol. 69, pp. 111–121). Elsevier Ltd. https://doi.org/10.1016/j.semcdb.2017.07.040

Lefebvre, J. L., Kostadinov, D., Chen, W. v., Maniatis, T., & Sanes, J. R. (2012). Protocadherins mediate dendritic self-avoidance in the mammalian nervous system. *Nature*, *488*(7412), 517–521. https://doi.org/10.1038/nature11305

Lefebvre, J. L., Sanes, J. R., & Kay, J. N. (2015). Development of Dendritic Form and Function. *Annual Review of Cell and Developmental Biology*, *31*, 741–777. https://doi.org/10.1146/annurev-cellbio-100913-013020

Malmierca, M. S., Seip, K. L., & Osen, K. K. (1995). Morphological classification and identification of neurons in the inferior colliculus: a multivariate analysis. *Anatomy and Embryology*, *191*(4), 343–350. https://doi.org/10.1007/BF00534687

Meza, R. C., López-Jury, L., Canavier, C. C., & Henny, P. (2018). Role of the axon initial segment in the control of spontaneous frequency of nigral dopaminergic neurons in vivo. *Journal of Neuroscience*, *38*(3), 733–744. https://doi.org/10.1523/JNEUROSCI.1432-17.2017

Michael Kleder. (2022). *Centroid of a Convex n-Dimensional Polyhedron*. https://www.mathworks.com/matlabcentral/fileexchange/8514-centroid-of-a-convex-n-dimensional-polyhedron

Mihaljević, B., Benavides-Piccione, R., Bielza, C., DeFelipe, J., & Larrañaga, P. (2015). Bayesian Network Classifiers for Categorizing Cortical GABAergic Interneurons. *Neuroinformatics*, *13*(2), 193–208. https://doi.org/10.1007/s12021-014-9254-1

Montero, T., Gatica, R. I., Farassat, N., Meza, R., González-Cabrera, C., Roeper, J., & Henny, P. (2021). Dendritic Architecture Predicts in vivo Firing Pattern in Mouse Ventral Tegmental Area and Substantia Nigra Dopaminergic Neurons. *Frontiers in Neural Circuits*, *15*. https://doi.org/10.3389/fncir.2021.769342

Muller, D. E., & Preparata, F. P. (1978). Finding the intersection of two convex polyhedra. *Theoretical Computer Science*, *7*(2), 217–236. https://doi.org/https://doi.org/10.1016/0304-3975(78)90051-8

Nedelescu, H., Abdelhack, M., & Pritchard, A. T. (2018). Regional differences in Purkinje cell morphology in the cerebellar vermis of male mice. *Journal of Neuroscience Research*, *96*(9), 1476–1489. https://doi.org/10.1002/jnr.24206

Nieuwenhuys, R., Donkelaar, H. J., & Nicholson, C. (1998). *The Central Nervous System of Vertebrates: With Posters* (Issue v. 1-3). Springer.

Oleson, E. B., Cachope, R., Fitoussi, A., Tsutsui, K., Wu, S., Gallegos, J. A., & Cheer, J. F. (2014). Cannabinoid Receptor Activation Shifts Temporally Engendered Patterns of Dopamine Release. *Neuropsychopharmacology*, *39*(6), 1441–1452. https://doi.org/10.1038/npp.2013.340

Packer, A. M., McConnell, D. J., Fino, E., & Yuste, R. (2013). Axo-dendritic overlap and laminar projection can explain interneuron connectivity to pyramidal cells. *Cerebral Cortex (New York, N.Y.: 1991)*, *23*(12), 2790–2802. https://doi.org/10.1093/cercor/bhs210

Peters, A., & Feldman, M. L. (1976). The projection of the lateral geniculate nucleus to area 17 of the rat cerebral cortex. I. General description. *Journal of Neurocytology*, *5*(1), 63–84. https://doi.org/10.1007/BF01176183

Phillipson, O. T. (1979). A Golgi study of the ventral tegmental area of Tsai and interfascicular nucleus in the rat. *Journal of Comparative Neurology*, *187*(1), 99–115. https://doi.org/10.1002/cne.901870107

Ramon y Cajal, S. (1904). *Textura del sistema nervioso del hombre y de los vertebrados: estudios sobre el plan estructural y composición histológica de los centros nerviosos adicionados de consideraciones fisiológicas fundadas en los nuevos descubrimientos* (Issue v. 2,n.°2). N. Moya.

Ramón-Moliner, E., & Nauta, W. J. H. (1966). The isodendritic core of the brain stem. *Journal of Comparative Neurology*, *126*(3), 311–335. https://doi.org/10.1002/cne.901260301

Rice, M. E., & Patel, J. C. (2015). Somatodendritic dopamine release: Recent mechanistic insights. *Philosophical Transactions of the Royal Society B: Biological Sciences*, *370*(1672), 1–14. https://doi.org/10.1098/rstb.2014.0185

Rojo, C., Leguey, I., Kastanauskaite, A., Bielza, C., Larrañaga, P., Defelipe, J., & Benavides-Piccione, R. (2016). Laminar Differences in Dendritic Structure of Pyramidal Neurons in the Juvenile Rat Somatosensory Cortex. *Cerebral Cortex*, *26*(6), 2811–2822. https://doi.org/10.1093/cercor/bhv316

Rotterman, T. M., Nardelli, P., Cope, T. C., & Alvarez, F. J. (2014). Normal distribution of VGLUT1 synapses on spinal motoneuron dendrites and their reorganization after nerve injury. *Journal of Neuroscience*, *34*(10), 3475–3492. https://doi.org/10.1523/JNEUROSCI.4768-13.2014

Takeo, Y. H., Shuster, S. A., Jiang, L., Hu, M. C., Luginbuhl, D. J., Rülicke, T., Contreras, X., Hippenmeyer, S., Wagner, M. J., Ganguli, S., & Luo, L. (2021). GluD2- and Cbln1-mediated competitive interactions shape the dendritic arbors of cerebellar Purkinje cells. *Neuron*, *109*(4), 629-644.e8. https://doi.org/10.1016/j.neuron.2020.11.028

822 Tang, M., Miyamoto, Y., & Huang, E. J. (2009). Multiple roles of β-catenin in controlling the
823 neurogenic niche for midbrain dopamine neurons. *Development*, *136*(12), 2027–2038.
824 https://doi.org/10.1242/dev.034330
825 Vrieler, N., Loyola, S., Yarden-Rabinowitz, Y., Hoogendorp, J., Medvedev, N., Hoogland, T. M., de
826 Zeeuw, C. I., de Schutter, E., Yarom, Y., Negrello, M., Torben-Nielsen, B., & Uusisaari, M. Y.
827 (2019). Variability and directionality of inferior olive neuron dendrites revealed by detailed
828 3D characterization of an extensive morphological library. *Brain Structure and Function*,
829 *224*, 1677–1695. https://doi.org/10.1007/s00429-019-01859-z
830 Zhang, L., Song, N.-N., Chen, J.-Y., Huang, Y., Li, H., & Ding, Y.-Q. (2012). Satb2 Is Required for
831 Dendritic Arborization and Soma Spacing in Mouse Cerebral Cortex. *Cerebral Cortex*, *22*(7),
832 1510–1519. https://doi.org/10.1093/cercor/bhr215
833
834

835 **Figure 1**. **Dendritic domain intersection.** A) A pair of reconstructed VTA DA neurons (left) and
836 their corresponding CHPs (center). The intersected volume is shown in darker gray volume
837 (right). Cell bodies are represented with discs. B) All CHPs of VTA DA neurons used in this study
838 (n = 15, frontal view only), numbered. Cell bodies are represented with discs.

839 **Figure 2. Validation of CHP intersection.** A1) Correlation between CHP volume and dendritic
840 length from a sample of VTA DA neurons (n = 15). Spearman correlation was used. Line
841 represents a linear regression. A2) Schematic illustrating the 3D wedge analysis, for dendritic
842 length (left) and CHP volume (right). Dendritic length was measured in each quadrant and
843 normalized using the total dendritic length of the neuron. For the CHP wedge analysis, the
844 volume of the CHP in each quadrant was measured and normalized by the total CHP volume.
845 Dendrites or CHP wedges inside the anterior or posterior plane were colored orange or cyan,
846 respectively. A3) Distribution of dendritic trees and CHP volume for VTA DA neurons (n = 15
847 neurons), in the anterior (left) and posterior (right) quadrants. When a two-way ANOVA was
848 performed, no significant differences were found: Interaction: Anterior quadrants, $F_{(3,42)}$=
849 0.8531, p=0.4729; Posterior quadrants, $F_{(3,42)}$= 0.8369, p=0.4813. Bars represent mean $\pm$ SEM.
850 B1) Representative example of a pair of VTA DA neurons whose CHPs intersect (left, mirrored
851 frontal view, reflected for layout porpuses). Inside the intersected volume, dendrites from both
852 neurons are found (right). The nearest neighbor distance between dendritic points of the pair
853 of neurons is depicted (black dotted line). B2) Distribution of nearest neighbor values between
854 pair of dendrites inside CHP intersection (n = 64 pairs of CHPs). B3) Correlation between the
855 intersected volume and the dendritic length inside intersection (n = 64 pairs of CHPs).
856 Spearman correlation was used. Line represents a linear regression.

857 **Figure 3. CHP intersection dynamics.** A) Example of a pair of VTA DA neurons CHPs (frontal
858 view, numbers relate to Figure 1B) that were initially centered in their cell bodies (black disc)
859 and following the displacement of one of the neuron CHP (3) across the ML axis. Intersected
860 volume is shown in darker gray. Cell bodies are represented with discs. B) Representative
861 examples of IR analysis between all pairs of VTA DA neurons across the ML, DV and AP axes. IR
862 was tested from 0 to 400 µm, in 10 µm steps. In this Figure, depicted pairs are indicated by
863 their respective numbers in Figure 1B).: First number corresponded to the neuron CHP that
864 stayed in a fixed position, second number corresponded to the neuron CHP that was moved
865 across the axis. Note the diversity of intersection dynamics observed.
866
867 **Figure 4. Modeling of neuron CHPs intersection dynamics.** A) Original, unmodified pair of VTA
868 DA neurons CHPs. Numbers inside are related to Figure 1B. CHP volume is depicted inside each
869 CHP. Cell bodies are represented as discs. B) Normalized volume modeling: in a given
870 population of neurons CHPs (A), the average CHP volume was obtained (in this case, the
871 average of the pair, 0.046 mm^3) and then all the neurons CHPs were normalized to that average
872 CHP volume. C) Normalized shape modeling: first, neurons CHPs were centered, using their cell
873 bodies as reference (represented as discs). Then, the normalized shape was obtained (more
874 details in methods and Supplementary Figure 1). Following, new CHPs were obtained from this
875 normalized shape, using the original CHPs volumes of the neurons. D) Normalized cell body
876 position: in a given population of neurons CHPs (A), the centroid of each CHP was obtained and
877 used as the reference for that CHP (black discs).
878 **Figure 5. Normalized CHP shape for different neuronal types.** The normalized CHP shape was

879 obtained for: A) VTA DA neurons (mouse); B) cerebellar Purkinje neurons (PC, mouse), SNc DA
880 neurons (mouse and rat), mediodorsal thalamic neurons (MD, rat) and spinal motoneurons
881 (MN, rat). The volume for each normalized shape was modifed to match the average CHP
882 volume of the corresponding sample. Neurons are shown from the frontal, lateral and dorsal
883 views. Cell bodies are represented with discs.

884 **Figure 6. CHP modeling for VTA DA neurons.** A1-3) IR vs distance plots across the ML (A1), DV (
885 A2) and AP (A3) axes were performed for all the possible pairs of VTA DA neurons (210 pairs per
886 distance) and compared between modeling conditions. IR was measured between 0 to 400 µm
887 (10 µm steps). Discontinuous color horizontal lines on the top of each plot depict the significant
888 differences ($p < 0.05$, Wilcoxon signed rank test with Sidak multiple comparisons correction)
889 between original vs normalized volume (black and cyan line), original vs normalized cell body
890 (black and red line), original vs normalized shape (black and orange line), normalized volume vs
891 normalized cell body (cyan and red line), normalized volume vs normalized shape (cyan and
892 orange line), and normalized cell body vs normalized shape (red and orange line). Solid line
893 represents the median. Error bars are omitted (data with error bars are shown in
894 Supplementary Figure 2). B1-3) Comparison between normalized shape modeling for VTA DA
895 neurons vs average neurons according to isotropy index, morphology, and wedge dendritic
896 distribution analysis (details in methods). Discontinuous color horizontal lines on the top of
897 each plot depict the significant differences ($p < 0.05$, Wilcoxon signed rank test with Sidak
898 multiple comparisons correction) between original vs average isotropy index (black and
899 magenta line), original vs average morphology (black and red line), and original vs average
900 wedge (black and orange) neurons. Solid line represents the median. Error bars are omitted.

901 **Figure 7. CHP modeling: examples from different neuronal types.** A1-3) Original data analysis:
902 IR vs distance plots across the ML (A1), DV (A2) and AP (A3) axes were performed for all the
903 possible pairs of SNc DA neurons (mouse and rat), cerebellar Purkinje neurons (PC, mouse),
904 mediodorsal thalamic neurons (MD, rat) and spinal motoneurons (MN, rat). Solid lines
905 represent the median. Error bars were omitted. B1-6) Within region modeling analysis: IR vs
906 distance plots are shown for modeling conditions of: SNc DA neurons (mouse), ML axis (B1);
907 SNc DA neurons (rat), ML axis (B2); Mediodorsal thalamic neurons (rat), ML axis (B3), spinal
908 motoneurons (rat), ML axis (B4), cerebellar Purkinje neurons (mouse), ML (B5') and AP (B5'')
909 axes. IR was measured between 0 to 400 µm (10 µm steps). Discontinuous color horizontal lines
910 on the top of each plot depict the significant differences ($p < 0.05$, Wilcoxon signed rank test
911 with Sidak multiple comparisons correction) between original vs normalized volume (black and
912 cyan line), original vs normalized cell body position (black and red line), original vs normalized
913 shape (black and orange), normalized volume vs normalized cell body position (cyan and red
914 line), normalized volume vs normalized shape (cyan and orange line), and normalized cell body
915 position vs normalized shape (red and orange line). Solid line represents the median. Error bars
916 are omitted.

917 **Figure 8. CHP intersection analysis: VTA DA neurons in their original brain position.** A1-2)
918 Rendered 3D map of the VTA, showing the cell bodies (A1) and cell bodies plus their dendrites
919 (A2) of the 15 VTA DA neurons, as in their real positions in the VTA (determined in (Montero et
920 al., 2021)), and seen in frontal (first row) and dorsal (second row) views. B1-4) IR vs distance
921 plots of the 105 possible pairs of VTA DA neurons, as tested unmodified (original, B1) and with
922 CHP normalized volume (B2), normalized shape (B3), and normalized cell body location (B4).

923 Each point represents the IR value of a pair of CHPs. Black line corresponds to an exponential
924 decay non-linear regression. C1-2) IR values from (B) were grouped according to their distance
925 between cell bodies: 50% closer distances (C1, n = 53) and 50% of farther distances (C2, n = 52)
926 between cell bodies. Data are represented as box and whiskers, showing the median (middle
927 line) and the 25th and 75th percentile in the box and the lowest and highest values (whiskers).
928 * $p < 0.05$, *** $p < 0.001$ using a Friedman test followed by a Dunn's multiple comparisons test.
929

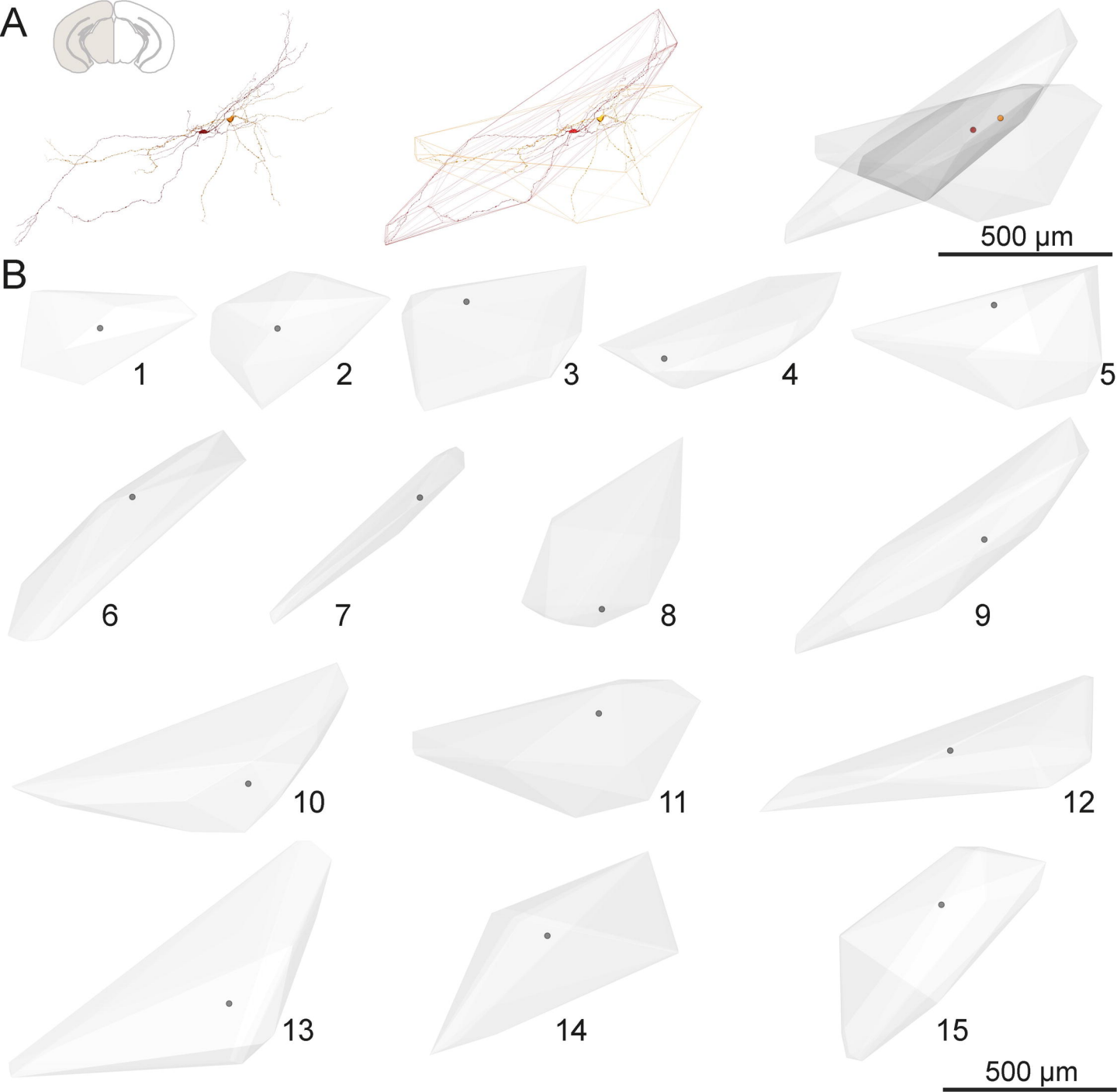
A
500 µm
B
1
2
3
4
5
6
7
8
9
10
11
12
13
14
15
500 µm

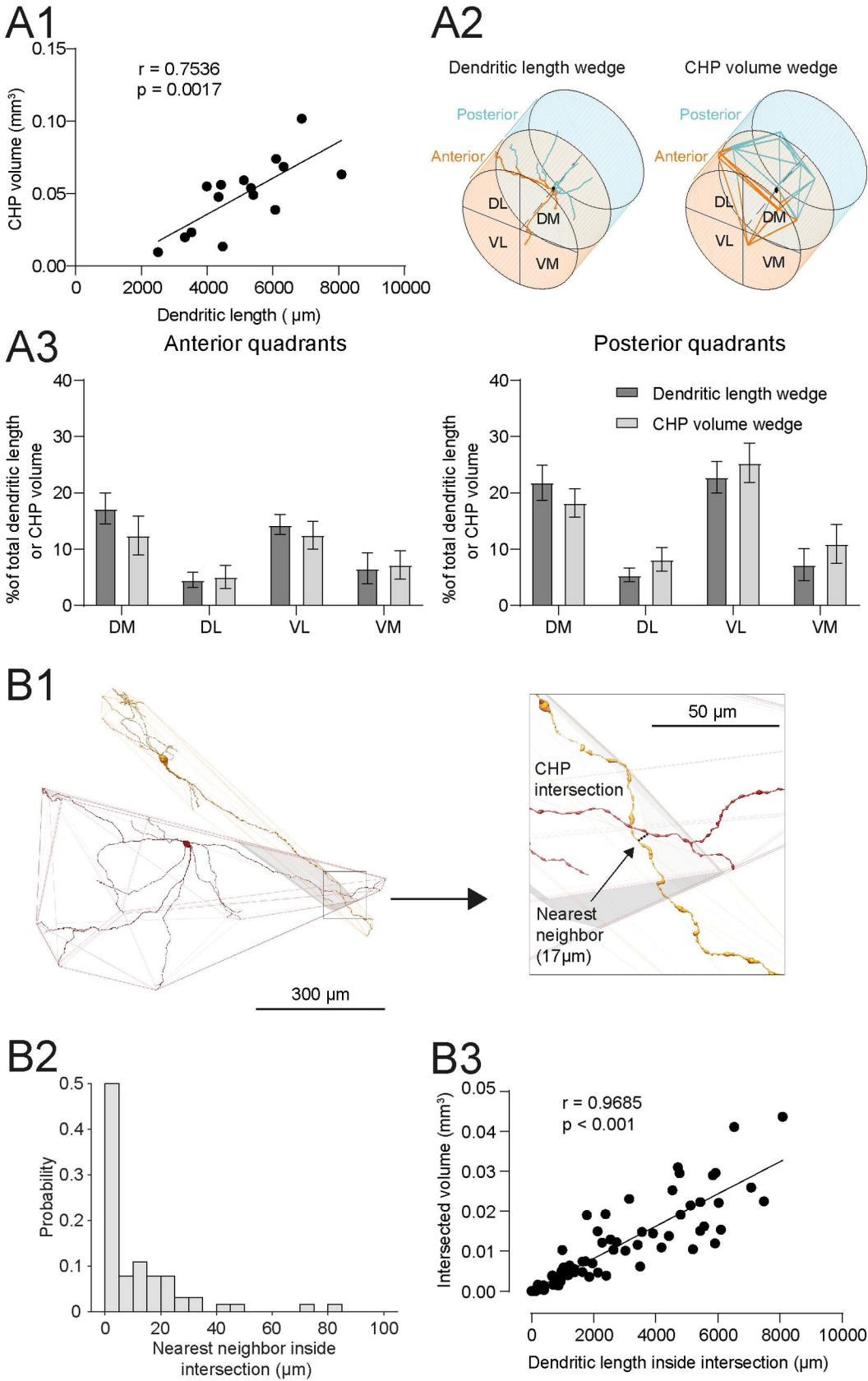
A1
r = 0.7536
p = 0.0017
CHP volume (mm³)
Dendritic length (µm)
A2
Dendritic length wedge
CHP volume wedge
Posterior
Anterior
DL
DM
VL
VM
A3
Anterior quadrants
Posterior quadrants
Dendritic length wedge
CHP volume wedge
%of total dendritic length or CHP volume
DM
DL
VL
VM
B1
50 µm
CHP intersection
Nearest neighbor (17µm)
300 µm
B2
Probability
Nearest neighbor inside intersection (µm)
B3
r = 0.9685
p < 0.001
Intersected volume (mm³)
Dendritic length inside intersection (µm)

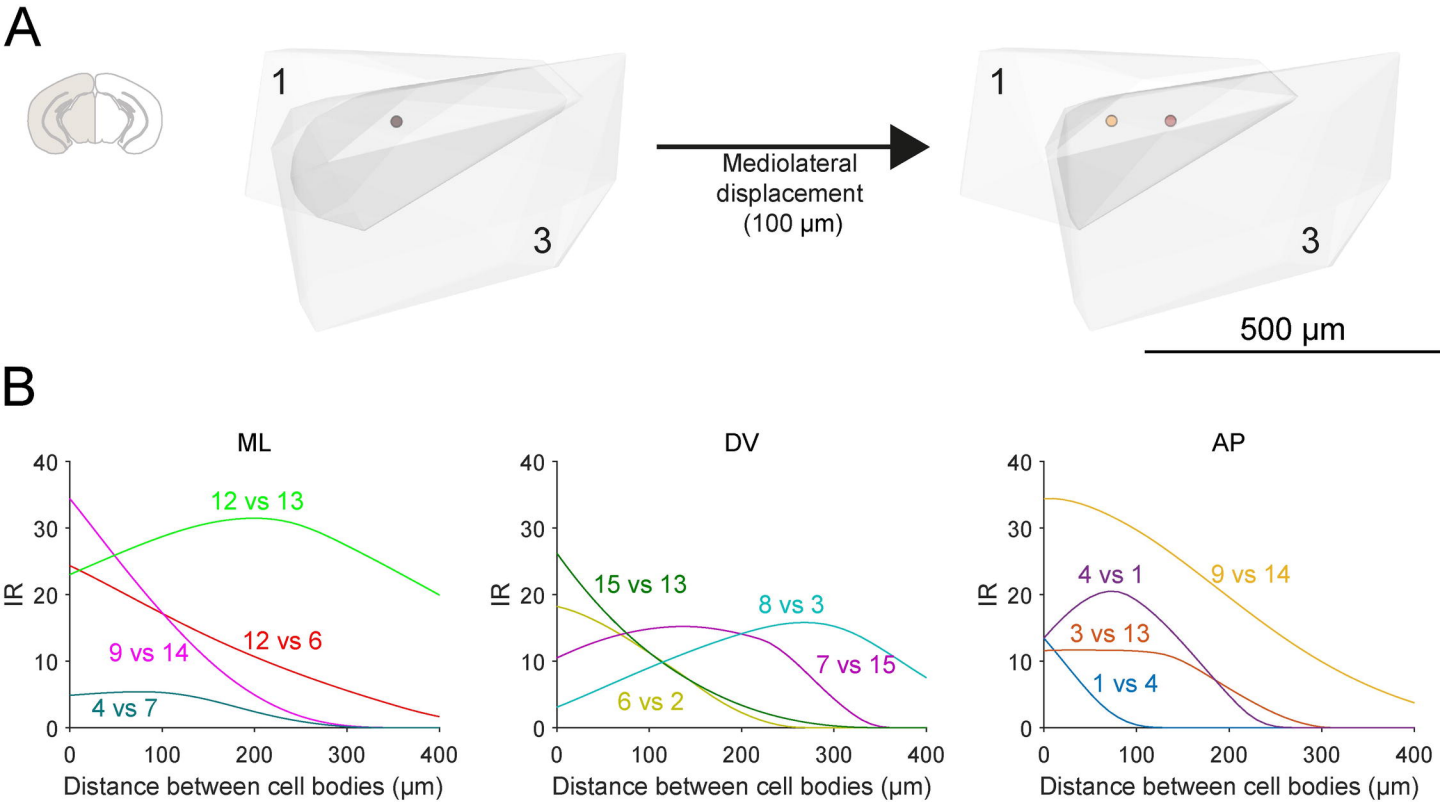
A
1
3
Mediolateral
displacement
(100 µm)
1
3
500 µm
B
ML
DV
AP
IR
Distance between cell bodies (µm)
12 vs 13
12 vs 6
9 vs 14
4 vs 7
15 vs 13
8 vs 3
7 vs 15
6 vs 2
4 vs 1
9 vs 14
3 vs 13
1 vs 4
0
10
20
30
40
0
100
200
300
400

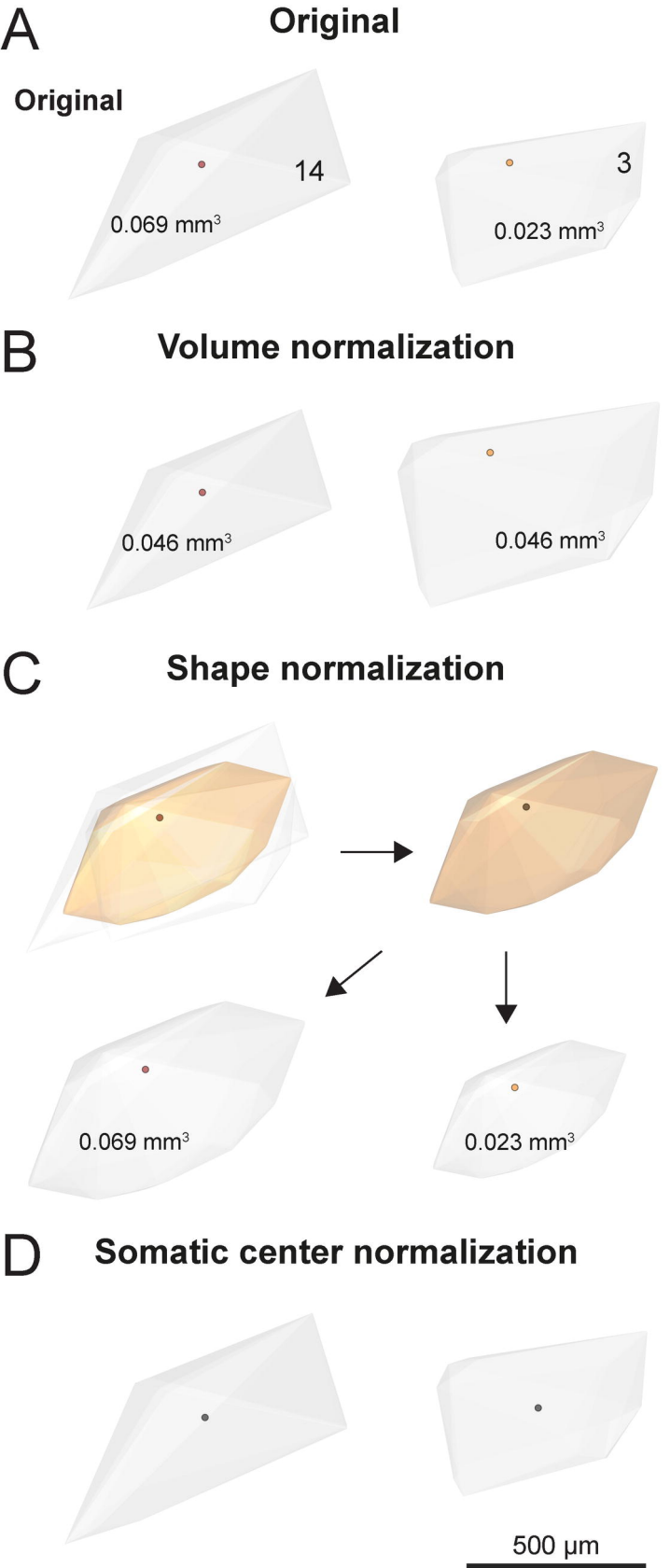
A
Original
Original
14
0.069 mm3
3
0.023 mm3
B
Volume normalization
0.046 mm3
0.046 mm3
C
Shape normalization
0.069 mm3
0.023 mm3
D
Somatic center normalization
500 µm

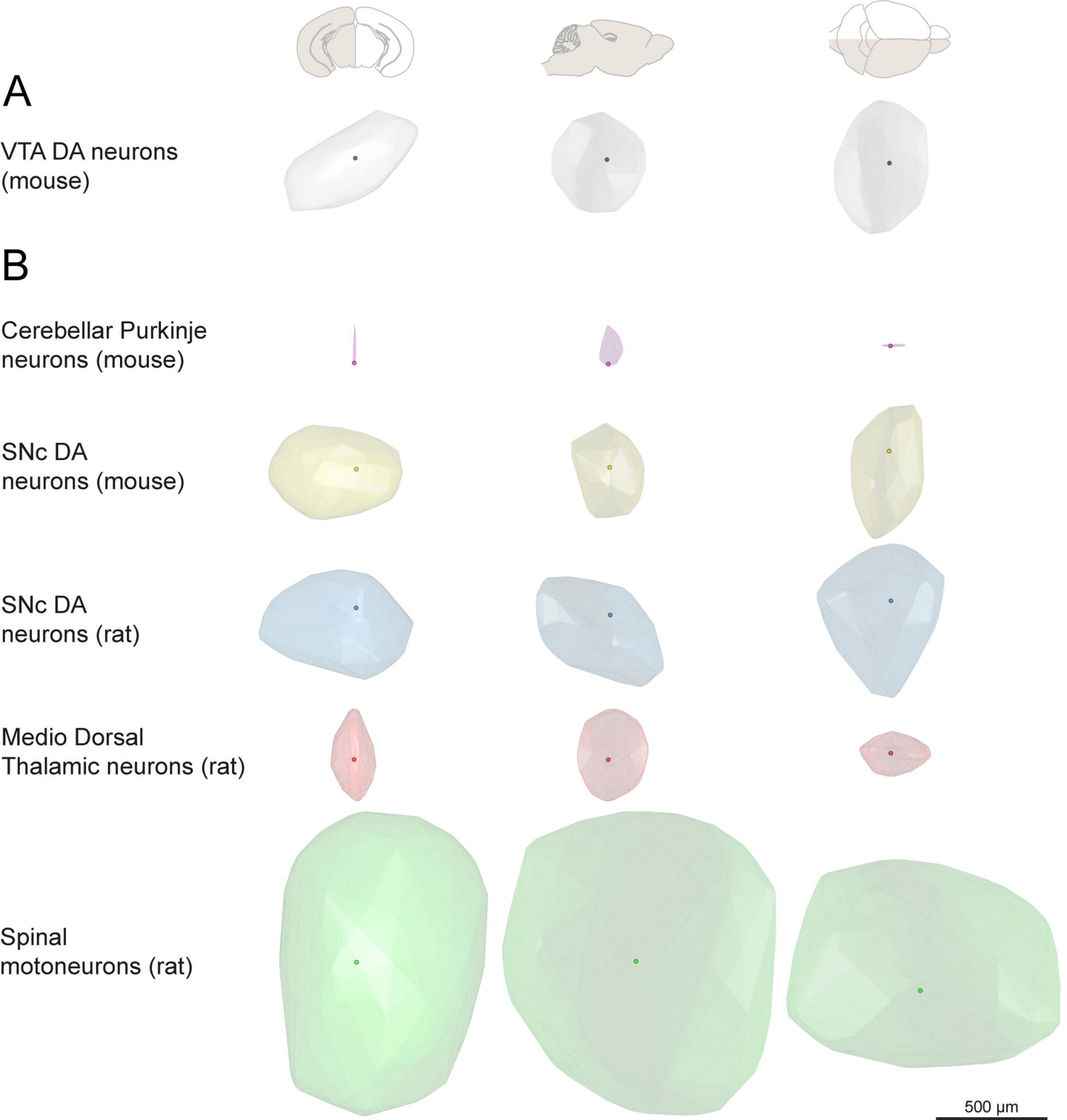
A
VTA DA neurons
(mouse)
B
Cerebellar Purkinje
neurons (mouse)
SNc DA
neurons (mouse)
SNc DA
neurons (rat)
Medio Dorsal
Thalamic neurons (rat)
Spinal
motoneurons (rat)
500 µm

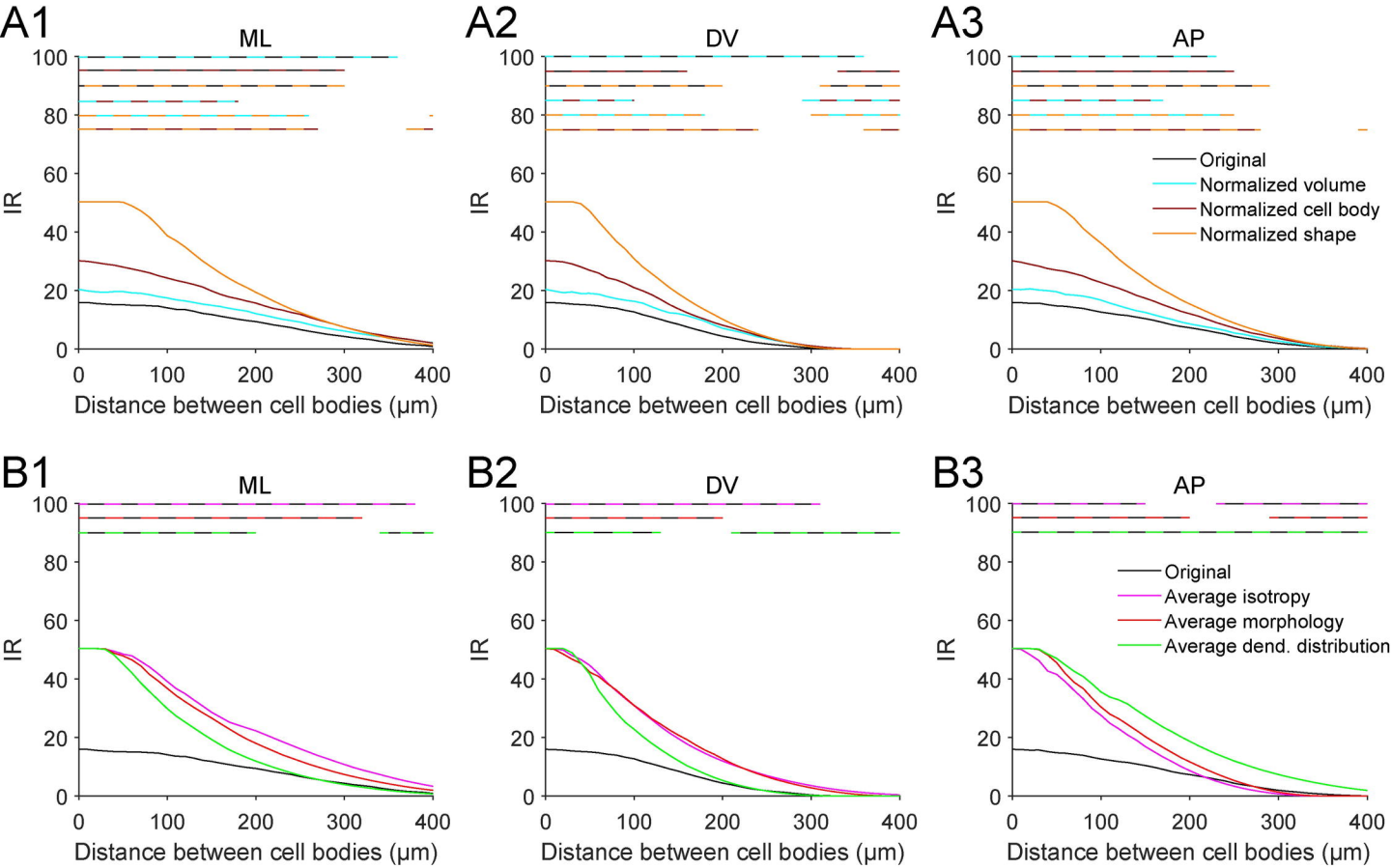
A1
ML
A2
DV
A3
AP
IR
Distance between cell bodies (μm)
Original
Normalized volume
Normalized cell body
Normalized shape
B1
ML
B2
DV
B3
AP
Original
Average isotropy
Average morphology
Average dend. distribution

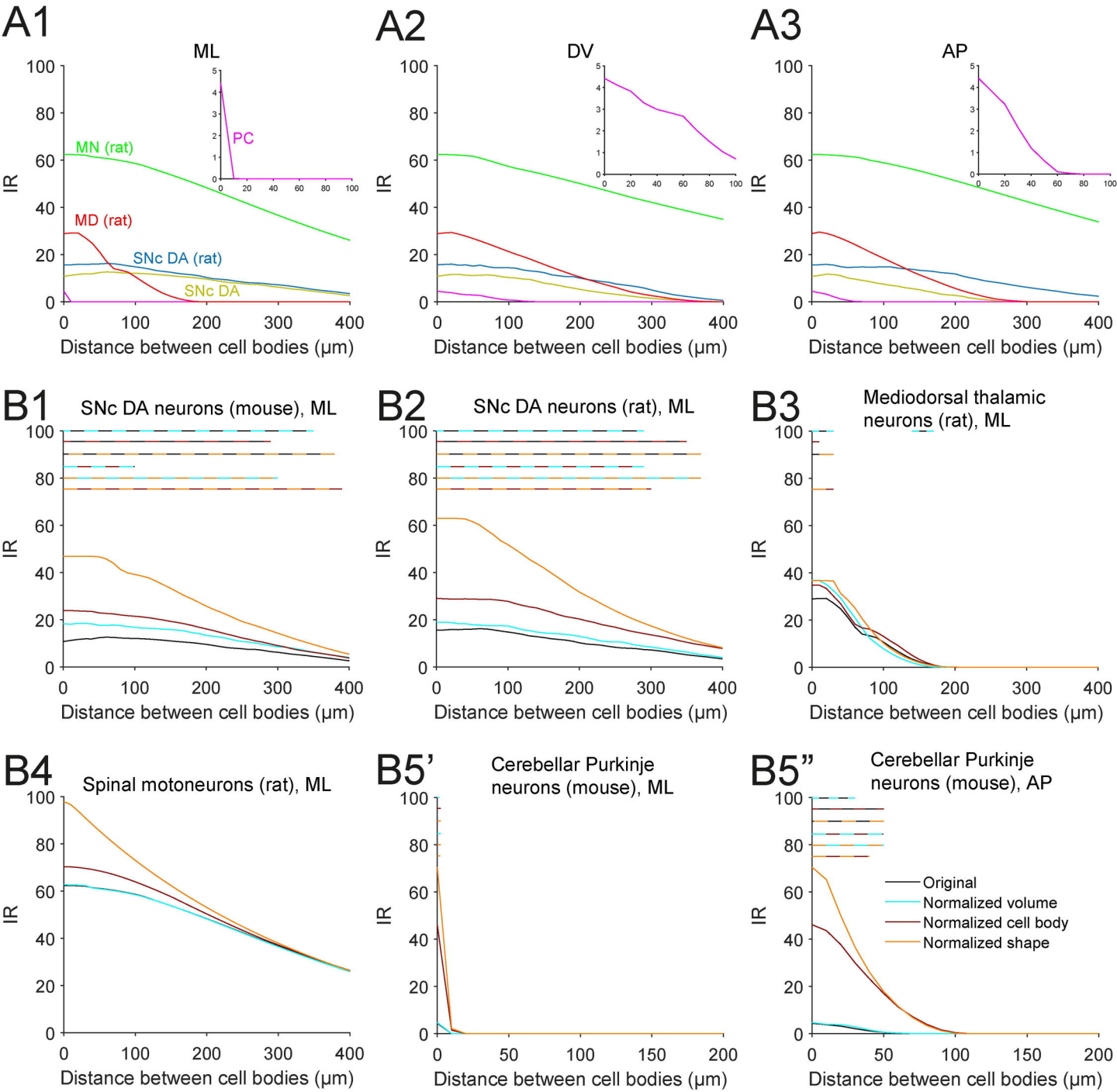
A1
ML
MN (rat)
PC
MD (rat)
SNc DA (rat)
SNc DA
IR
Distance between cell bodies (μm)
A2
DV
A3
AP
B1
SNc DA neurons (mouse), ML
B2
SNc DA neurons (rat), ML
B3
Mediodorsal thalamic neurons (rat), ML
B4
Spinal motoneurons (rat), ML
B5'
Cerebellar Purkinje neurons (mouse), ML
B5"
Cerebellar Purkinje neurons (mouse), AP
Original
Normalized volume
Normalized cell body
Normalized shape

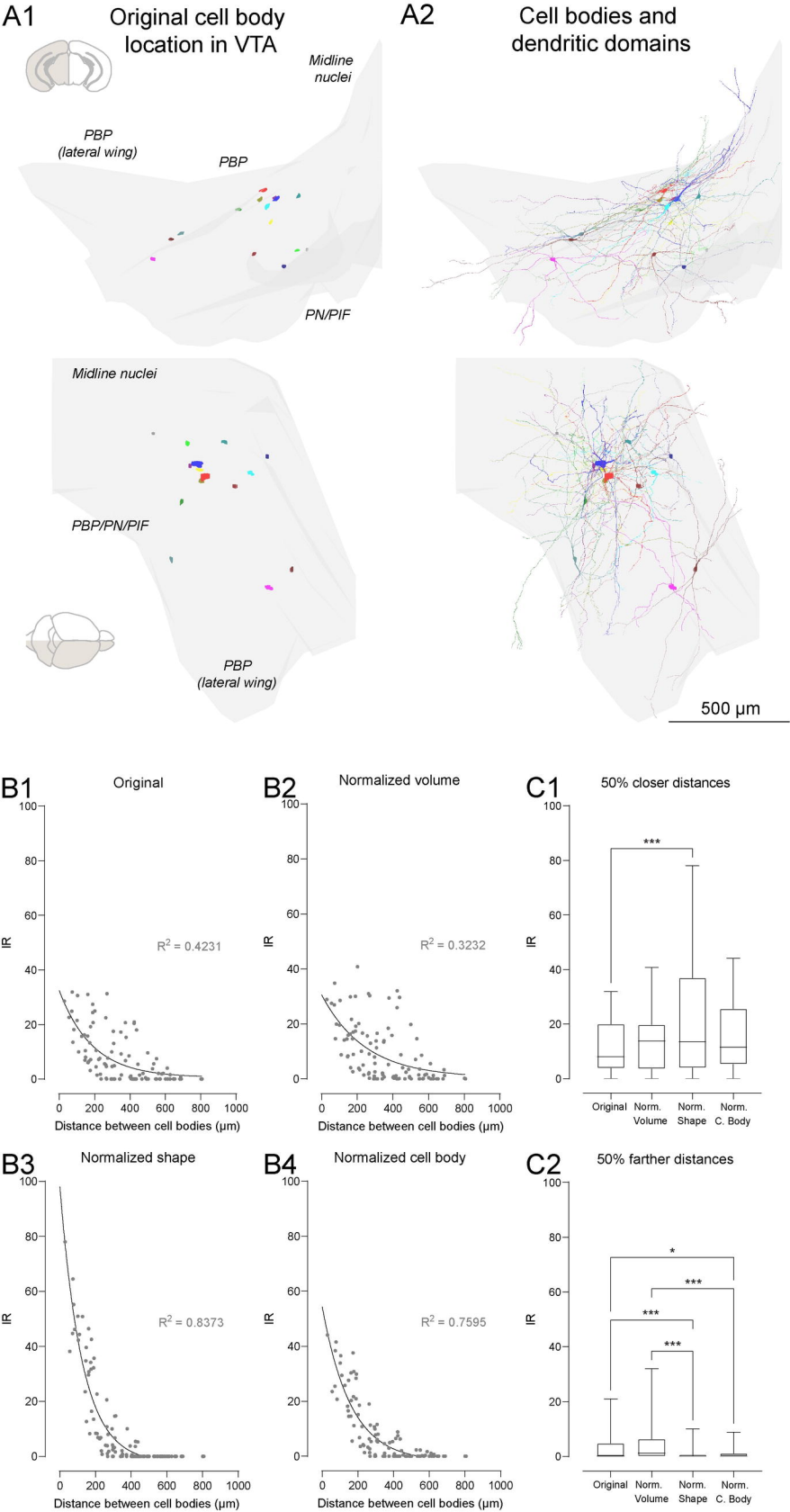
A1
Original cell body location in VTA
Midline nuclei
PBP (lateral wing)
PBP
PN/PIF
Midline nuclei
PBP/PN/PIF
PBP (lateral wing)
A2
Cell bodies and dendritic domains
500 µm
B1
Original
R² = 0.4231
B2
Normalized volume
R² = 0.3232
C1
50% closer distances
***
B3
Normalized shape
R² = 0.8373
B4
Normalized cell body
R² = 0.7595
C2
50% farther distances
*
***
***
***
IR
Distance between cell bodies (µm)
Original
Norm. Volume
Norm. Shape
Norm. C. Body